Remote Sensing of Environment 219 (2018) 233–246

Contents lists available at ScienceDirect

Remote Sensing of Environment

journal homepage: www.elsevier.com/locate/rse

Reconstruction of the full spectrum of solar-induced chlorophyll fluorescence: Intercomparison study for a novel method

Feng Zhao[a,b,*,1], Rong Li[a], Wout Verhoef[c], Sergio Cogliati[d], Xinjie Liu[e], Yanbo Huang[f], Yiqing Guo[g], Jianxi Huang[h,b]

[a] School of Instrumentation Science and Opto-Electronics Engineering, Beihang University, Beijing, 100083, PR China
[b] Key Laboratory of Remote Sensing for Agri-Hazards, Ministry of Agriculture and Rural Affairs, Beijing, 100083, PR China
[c] Faculty of Geo-information Science and Earth Observation (ITC), University of Twente, P.O. Box 217, Enschede 7500 AE, the Netherlands
[d] Remote Sensing of Environmental Dynamics Lab., DISAT, University of Milano-Bicocca, 20126 Milano, Italy
[e] Key Laboratory of Digital Earth Science, Institute of Remote Sensing and Digital Earth, Chinese Academy of Sciences, Beijing, 100094, PR China
[f] United States Department of Agriculture-Agricultural Research Service, Crop Production Systems Research Unit, 141 Experiment Station Road, Stoneville, MS 38776, USA
[g] School of Engineering and Information Technology, The University of New South Wales, Canberra ACT 2600, Australia
[h] College of Land Science and Technology, China Agricultural University, Beijing 100083, PR China

ARTICLE INFO

Keywords:
Solar-induced chlorophyll fluorescence (SIF)
The full SIF spectrum
Fluorescence spectrum reconstruction
FLEX mission
Intercomparison
Basis spectra
Spectral fitting
SCOPE
FluorWPS

ABSTRACT

Solar-Induced chlorophyll Fluorescence (SIF) can serve as an early and non-invasive indicator of the functioning and status of vegetation due to its close link to photosynthetic activity. Most existing approaches retrieve SIF at around few discrete absorption lines. However, the full SIF spectrum can provide more information on the functional status of photosynthetic machinery. European Space Agency's FLuorescence EXplorer (FLEX) mission, to be launched in 2022, is dedicated to the accurate reconstruction of the full SIF spectrum over land and incorporates the heights and positions of the two SIF peaks and the total fluorescence emission (spectrally-integrated value) into planned Level-2 products.

In this paper, an advanced Fluorescence Spectrum Reconstruction (aFSR) method was proposed to reconstruct the full SIF spectrum by capitalizing on the features of existing methods. The aFSR method used linear combinations of basis spectra to approximate the spectra of SIF and the reflectance factor and exploited all available bands within the spectral range of SIF emission for spectral fitting of SIF and reflected radiance. The number of basis spectra of the reflectance factor used was self-adaptively determined based on the Bayesian information criterion. A comprehensive intercomparison between the aFSR method and three other methods (i.e., the Fluorescence Spectrum Reconstruction method, the Full-spectrum Spectral Fitting Method, and the SpecFit method) was performed using simulated and experimental datasets. For simulated datasets, the impact of spectral resolution (SR), signal-to-noise ratio (SNR), atmospheric correction, canopy structure, leaf biochemical parameters and directional effect on the accuracy of SIF spectrum reconstruction was considered. Results show that while all methods could achieve the accuracy standard set by the FLEX mission (average absolute relative error of spectrally-integrated SIF $< 10\%$) when spectral resolving power and SNR were high (e.g., SR ≤ 0.3 nm and SNR ≥ 700), aFSR generally provided the highest reconstruction accuracy. For the first time we investigated the performance of the SIF spectrum reconstruction on 3-D radiative transfer (RT) simulations and compared with that on typical 1-D simulations. The increase of canopy heterogeneity from 1-D to 3-D did not noticeably deteriorate the accuracy of aFSR, implying that aFSR was applicable to different canopy structures. The aFSR method was also more robust than other methods as it was less affected by atmospheric correction and directional effect. For the experimental dataset, the SIF spectra reconstructed by aFSR agreed well with literature in terms of shape, magnitude and diurnal variation and were in agreement with the other methods: the coefficient of determination and the root-mean-square error between the reconstruction results of aFSR and the average of the SIF spectra reconstructed through three other methods were higher than 0.93 and lower than 0.09 $W \cdot m^{-2} \cdot sr^{-1} \cdot \mu m^{-1}$, respectively.

* Corresponding author at: School of Instrumentation Science and Opto-Electronics Engineering, Beihang University, Beijing 100083, PR China.
E-mail address: zhaofeng@buaa.edu.cn (F. Zhao).

[1] The computer codes of the aFSR method (in Matlab) are available upon request.

https://doi.org/10.1016/j.rse.2018.10.021
Received 1 February 2018; Received in revised form 19 September 2018; Accepted 14 October 2018
Available online 17 October 2018
0034-4257/

1. Introduction

Solar-Induced chlorophyll Fluorescence (SIF) is an electromagnetic signal emitted by chlorophyll molecules after the absorption of solar radiation (Porcar-Castell et al., 2014). It is one of the three dissipation pathways for the absorbed solar light energy: the energy can be used to drive photosynthesis, excess energy is re-emitted as SIF or dissipated as heat (Maxwell and Johnson, 2000). The three processes are closely interrelated. Therefore, SIF carries plant physiological information, and it can serve as a direct and non-invasive indicator of the functional status of photosynthetic machinery (Malenovsky et al., 2009; Meroni et al., 2009; Rascher et al., 2015). SIF has been used to estimate gross primary production (Guanter et al., 2014; Zhang et al., 2014; Damm et al., 2015; Zhang et al., 2016; Sun et al., 2017) and detect plant stress in an early stage (Meroni et al., 2008; Ač et al., 2015; Rossini et al., 2015).

SIF is emitted in the spectral range of 640–850 nm and is characterized by two peaks centered at around 685 nm and 740 nm, respectively (Meroni et al., 2009). It is superimposed on the signal of scattered solar radiation and thus cannot be measured directly. The decoupling of the SIF signal from scattered radiation is challenging, also since the SIF radiance generally constitutes only a small fraction (1–5% in the near-infrared) of the upwelling radiance reaching the sensor (Meroni et al., 2009).

Despite these difficulties, there are several algorithms that allow to retrieve SIF signal. For a complete review, please refer to Meroni et al. (2009). Since then, more strategies have been proposed to retrieve SIF radiance for airborne and spaceborne measurements (Joiner et al., 2011; Guanter et al., 2012; Rascher et al., 2015; Wolanin et al., 2015). Most of the algorithms retrieve SIF radiance at around few discrete solar or telluric absorption lines, e.g., the potassium (K) I solar Fraunhofer line at 656 nm, and the O_2-A and O_2-B telluric absorption lines centered at 687 nm and 761 nm, respectively.

However, the full chlorophyll fluorescence spectrum can provide more information than the fluorescence radiance at the few absorption lines. The ratio between the maximum fluorescence in the red and far-red regions of the chlorophyll fluorescence spectra under artificial illumination is shown to be affected by various physiological and environmental factors: it is closely related to leaf chlorophyll content (C_{ab}) due to the re-absorption of red fluorescence by chlorophyll (Buschmann, 2007), and it can also serve as an indicator of herbicide treatment (Rinderle and Lichtenthaler, 1988; Zhao et al., 2015a), chilling stress (Agati et al., 1996) and nitrogen deficiency (Ač et al., 2015). Recently, the red and far-red maxima of the SIF spectrum were retrieved from airborne hyperspectral imagery of mature loblolly and their ratio is found to be linearly related to canopy light use efficiency over the diurnal cycle (Middleton et al., 2017). Some other parameters derived from the full fluorescence spectra also showed their applications. The spectral position and full width at half maximum of the red and far-red peaks of the spectrum of laser-induced chlorophyll fluorescence, as well as the curve area, were shown to be related to nutrient stress (Subhash and Mohanan, 1997). Van Wittenberghe et al. (2013) found that the ratio between the peaks of fluorescence yield in the red and far-red regions is more effective than chlorophyll content in indicating the difference between low and high traffic emission exposure. Verrelst et al. (2016) performed a simulation study on the relationship between SIF and net photosynthesis of the canopy (NPC). It was found that the correlation between SIF at different wavelengths and NPC is higher when exploiting the full SIF spectrum than when using SIF at 1–4 discrete bands.

Because of the potentially wide applications of the SIF spectrum on quantifying photosynthetic activity and monitoring plant stress, European Space Agency (ESA)'s FLuorescence EXplorer (FLEX) mission (to be launched in 2022) is dedicated to the accurate reconstruction of the full SIF spectrum over land and incorporates the heights and positions of the two SIF peaks and the total fluorescence emission (spectrally-integrated value) into planned Level-2 (L2) products (ESA, 2015; Coppo et al., 2017; Drusch et al., 2017). As the first satellite mission specifically designed to retrieve the SIF signal, FLEX can observe globally at a spatial resolution of 300 m to address the scale of agricultural management units. Therefore, spatial dynamics of the SIF spectrum and photosynthesis can be studied with this data source.

Several methods have been proposed recently to reconstruct the full SIF spectrum. They can be classified into three categories depending on whether and how the atmospheric effect is considered. The first category consists of the Fluorescence Spectrum Reconstruction (FSR) method (Zhao et al., 2014) and the Full-spectrum Spectral Fitting Method (F-SFM) (Liu et al., 2015) for top-of-canopy (TOC) measured data. The FSR method retrieves SIF radiance at several absorption lines by the Spectral Fitting Method (Meroni et al., 2010) and uses linear combination of basis spectra to fit the retrieved SIF radiance. The F-SFM method introduces an iterative approach and uses the apparent reflectance factor outside the major absorption wells to approximate the reflectance factor inside and near those wells. It uses linear combination of basis spectra to fit the apparent reflectance factor outside the major absorption wells and SIF inside and near those wells. Cogliati et al. (2015b) proposed a two-step approach to reconstruct SIF spectra with top-of-atmosphere (TOA) measured data, which falls into the second category. Firstly, atmospheric correction is applied; then, the SpecFit method is used to reconstruct the full SIF spectrum. The SpecFit method can also be directly used for TOC measured data. It uses specific mathematical functions to model the spectra of SIF and the reflectance factor and applies curve fitting within the full spectral region of SIF emission. The third category inverts coupled radiative transfer (RT) models of surface-atmosphere systems to reconstruct SIF spectra with TOA measured data, as reported in the study by Verhoef et al. (2018). In this approach, the RT of atmosphere and vegetation are coupled to simulate TOA radiance. Then, by model inversion via multi-sensor optimization, the SIF spectrum was retrieved along with some important canopy parameters (e.g., chlorophyll content (C_{ab}) and leaf area index (LAI)).

As can be seen above, the FSR, F-SFM, and SpecFit methods can all be used to reconstruct the SIF spectrum from TOC measured or TOA atmospherically corrected data (detailed description of these methods can be found in the Supplementary Data). When determining the number of basis spectra to be used, the FSR and F-SFM methods introduce subjectivity. Besides, they do not fully exploit all available information compared to the SpecFit method. As to the SpecFit method, it uses more coefficients than the FSR and F-SFM methods to approximate the spectrum of SIF. However, it is challenging to accurately determine all the coefficients.

The present work overcomes the above limitations to reconstruct the SIF spectrum from TOC measured or TOA atmospherically corrected data. An advanced fluorescence spectrum reconstruction (aFSR) method was proposed by capitalizing on the features of the existing methods and introducing a criterion for adaptively determining the number of basis spectra of the reflectance factor to be used for the reconstruction. This method was evaluated with TOC measured and TOA atmospherically corrected data by systematic comparison with the FSR, F-SFM, and SpecFit methods. Three different simulated datasets and an experimental dataset were used for the evaluation, by considering the impacts of sensor spectral configurations of spectral resolution (SR) and signal-to-noised ratio (SNR), atmospheric correction, canopy structural and biophysical characteristics, and directional effects. The physically-based method by Verhoef et al. (2018) was not included here since it applies for TOA data rather than TOC measured or TOA atmospherically corrected data.

The rest of the paper is organized as follows: in Section 2, the aFSR method and the datasets used in this study are described; a comprehensive intercomparison of the aFSR method and three other methods is performed in Section 3; discussions on the comparison results are presented in Section 4; Section 5 gives the concluding remarks.

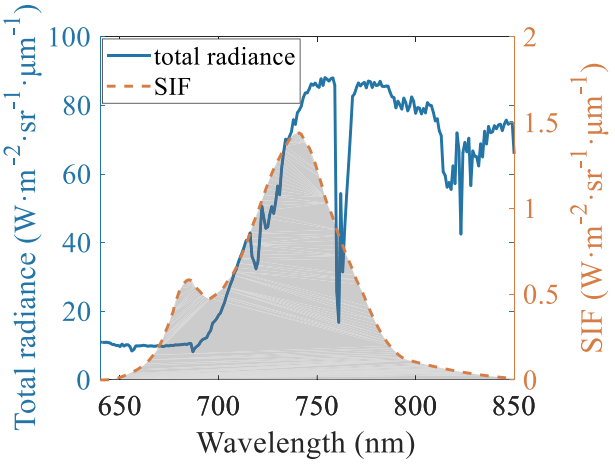

Fig. 1. Exemplary spectra of total upwelling radiance (blue solid line) and Solar-Induced chlorophyll Fluorescence (SIF) radiance (red dashed line) at top-of-canopy (TOC). The shaded region indicates the spectrally-integrated SIF. (For interpretation of the references to colour in this figure legend, the reader is referred to the web version of this article.)

2. Methods and materials

2.1. The advanced fluorescence spectrum reconstruction (aFSR) method

The TOC total upwelling radiance $L(\lambda)$ can be approximated by the following equation (Meroni et al., 2009):

$$L(\lambda) = \frac{E(\lambda)}{\pi} R(\lambda) + F(\lambda) \tag{1}$$

where λ is wavelength, and $E(\lambda)$, $R(\lambda)$ and $F(\lambda)$ are the incident irradiance, the canopy reflectance factor, and SIF, respectively. Fig. 1 shows the exemplary spectra of TOC total upwelling radiance (L) and SIF radiance (F). The shaded region indicates the spectrally-integrated SIF.

The aFSR method performs curve fitting within the full spectral region of SIF emission. The spectra of both the reflectance factor and SIF are modeled as linear combinations of basis spectra (a set of spectra extracted from training data with which one can fit any spectrum of the reflectance factor or SIF). Therefore, Eq. (1) becomes:

$$\widetilde{L}(\lambda) = \frac{E(\lambda)}{\pi} \sum_{i=1}^{N_r} c_{ri} \boldsymbol{\phi}_{ri}(\lambda) + \sum_{i=1}^{N_f} c_{fi} \boldsymbol{\phi}_{fi}(\lambda) \tag{2}$$

where $\widetilde{L}(\lambda)$ is the modeled total upwelling radiance, $\boldsymbol{\phi}_{ri}(\lambda)$ and $\boldsymbol{\phi}_{fi}(\lambda)$ are the basis spectra of the reflectance factor and SIF, respectively, c_{ri} and c_{fi} are the coefficients of the basis spectra to be determined, N_r and N_f are the numbers of basis spectra of the reflectance factor and SIF used, respectively.

To determine the coefficients (c_{ri} and c_{fi}), the optimization problem (weighted linear least squares) in Eq. (3) is solved with all available measurements between 640 nm and 850 nm.

$$\text{minimize} \sum_{\lambda=\lambda_1}^{\lambda_n} w(\lambda)[L(\lambda)-\widetilde{L}(\lambda)]^2 \tag{3}$$

where $L(\lambda)$ is the measured total upwelling radiance, and $w(\lambda)$ is the weight assigned to wavelength λ. $w(\lambda)$ is set as the reciprocal of the uncertainty of the radiance. In this study, sensor noise is considered as the only source of uncertainty, and $w(\lambda)$ can be calculated with SNR and measured radiance $L(\lambda)$ (Eq. (4)).

$$w(\lambda) = \frac{1}{u_n(\lambda)} = \frac{SNR(\lambda)}{L(\lambda)} \tag{4}$$

where $u_n(\lambda)$ is the uncertainty due to sensor noise.

The best N_f and N_r (using these numbers of basis spectra can provide the best reconstruction accuracy) can be different for different data, and the selection of N_f and N_r is not trivial. The best N_f for data with different combinations of SR and SNR obtained for the SCOPE dataset (to be introduced in Section 2.3.1) can be used as reference to select the proper N_fs for the reconstructions with other data. However, the proper N_r cannot be determined in a way similar to the determination of N_f because of its large range of variation and high uncertainty. To solve this problem, the Bayesian Information Criterion (BIC) (Schwarz, 1978) is adopted to self-adaptively select N_r. Under the assumption that the errors of modeled total upwelling radiance ($\widetilde{L}(\lambda)$) are independent and normally distributed, BIC can be calculated as (Schwarz, 1978):

$$\text{BIC} = n_\lambda \ln(RSS/n_\lambda) + k \ln(n_\lambda) \tag{5}$$

where n_λ is the number of wavelengths used, k is the number of coefficients to be determined and equals to $N_f + N_r$ (as mentioned above, N_f is already determined), and RSS is the residual sum of squares of total upwelling radiance. RSS is calculated as:

$$RSS = \sum_{\lambda=\lambda_1}^{\lambda_n} w(\lambda)[L(\lambda)-\widetilde{L}(\lambda)]^2 \tag{6}$$

BIC is calculated with different values of N_r, and the N_r corresponding to the smallest BIC is selected for the reconstruction. It was found that this method is not applicable to the determination of N_f.

Similarities and differences among the aFSR, FSR, F-SFM, and SpecFit methods are given in Table 1. More detailed comparisons of aFSR with the other three methods are presented in Section 4.2.

2.2. Training datasets and feature extraction of SIF and the reflectance factor

The aFSR, FSR, and F-SFM methods use training datasets for feature extraction (generation of basis spectra) of the SIF spectrum or spectra of both SIF and the reflectance factor. These training datasets were generated by the Soil Canopy Observation, Photochemistry and Energy fluxes model (SCOPE, version 1.60), which is an integrated model of RT and energy balance and can simulate the spectra of TOC outgoing

Table 1
Similarities and differences among the four SIF spectrum reconstruction algorithms.

Algorithm	Modeling of the SIF spectrum	Modeling of the spectrum of the reflectance factor	Optimization method	Other features
aFSR	Linear combination of basis spectra	Linear combination of basis spectra	Linear least squares	Directly applying curve fitting within the full spectral region of SIF emission; self-adaptively selecting the number of basis spectra of the reflectance factor
FSR	Linear combination of basis spectra	–	Linear least squares	Using the spectral fitting method to retrieve SIF radiance at several absorption lines
F-SFM	Linear combination of basis spectra	Linear combination of basis spectra	Linear least squares	Using the apparent reflectance factor outside the major absorption wells to approximate the reflectance factor inside and near those wells; introducing an iterative process
SpecFit	Pseudo-Voigt functions	Piecewise cubic spline function	Non-linear least squares	Directly applying curve fitting within the full spectral region of SIF emission

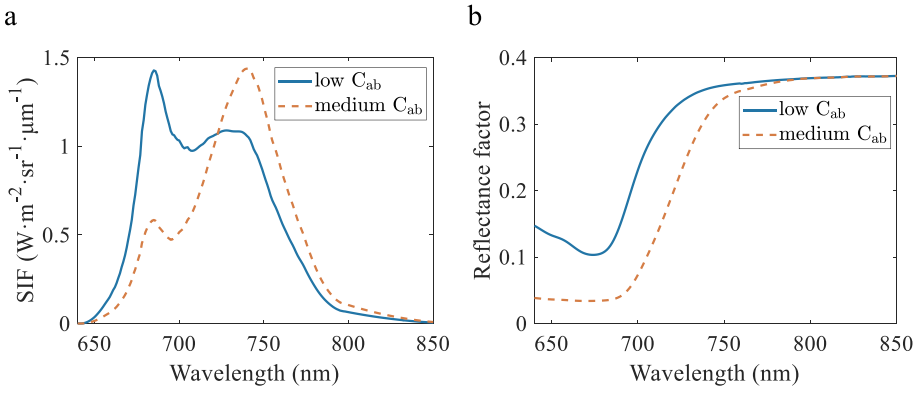

Fig. 2. a) Exemplary SIF spectra for canopies with low C_{ab} (5 μg·cm^{-2}, blue solid line) and medium C_{ab} (40 μg·cm^{-2}, red dashed line). b) Exemplary spectra of the reflectance factor for canopies with low C_{ab} (5 μg·cm^{-2}, blue solid line) and medium C_{ab} (40 μg·cm^{-2}, red dashed line). (For interpretation of the references to colour in this figure legend, the reader is referred to the web version of this article.)

radiance, the reflectance factor, and fluorescence radiance for homogeneous canopies (van der Tol et al., 2009). To make the training datasets representative of the majority of actual scenes, the cases were generated by randomly varying the 15 most influential SCOPE input parameters (Zhao et al., 2014; Verrelst et al., 2015) with a uniform distribution within their reasonable ranges.

Due to the re-absorption of red fluorescence by chlorophyll, the SIF spectra observed at TOC for canopies with low C_{ab} are quite different from those for canopies with medium or high C_{ab}, as shown in Fig. 2a for canopies with C_{ab} of 5 μg·cm^{-2} (low) and 40 μg·cm^{-2} (medium). Therefore, two different training datasets were simulated for extraction of basis spectra of TOC SIF. Training dataset I was generated for canopies with low C_{ab} (< 10 μg·cm^{-2}), and training dataset II for canopies with medium or high C_{ab} (≥ 10 μg·cm^{-2}). The threshold of 10 μg·cm^{-2} was chosen based on testing results (details can be found in the companioning Supplementary Data). However, the influence of C_{ab} on the spectrum of the reflectance factor is not as significant as on the SIF spectrum (Fig. 2b). Therefore, the training dataset for extraction of basis spectra of the TOC reflectance factor (referred to as training dataset III) was simulated without differentiation of C_{ab}.

Each of the three training datasets consists of 1600 spectra simulated for different cases. The spectra cover the range of 640–850 nm with both SR and spectral sampling interval (SSI) equal to 1 nm. The ranges of C_{ab} for the three datasets are listed in Table 2, while the definitions and ranges of the other 14 variables can be found in the Supplementary data. The remaining input parameters were fixed at their default values, and nadir viewing angle was used for all simulations.

The Singular Value Decomposition (SVD) technique (Press et al., 2007) was used to extract basis spectra from training datasets. Fig. 3 shows the first three basis SIF spectra (Fig. 3a and b) and the first four basis spectra of the reflectance factor (Fig. 3c). For canopies with low C_{ab}, the left peak of the first basis spectrum of SIF is higher than the right one (Fig. 3a), while the opposite is true for canopies with medium/high C_{ab} (Fig. 3b). It can be seen that the first basis spectra of SIF (BS1 of Fig. 3a–b) and the reflectance factor (BS1 of Fig. 3c) capture the dominate shapes of the spectra. The other basis spectra show some subtle features. For instance, the second and third basis SIF spectra can be used to adjust the peak-difference and the depth of the middle valley of the SIF spectrum, respectively.

Table 2
Ranges of the chlorophyll content for the three datasets.

	Range of chlorophyll content (μg·cm^{-2})
Training dataset I	0.4–10
Training dataset II	10–80
Training dataset III	0.4–80

2.3. Simulated test datasets

Three simulated datasets were generated to evaluate the reconstruction accuracies of the SIF spectra. The impacts of sensor spectral configurations (SR and SNR), atmospheric effect, canopy characteristics and directional effects were considered.

2.3.1. Dataset simulated by the SCOPE model

The performance of the SIF spectrum reconstruction under a wide range of sensor spectral configurations was evaluated by a test dataset simulated by the SCOPE model (referred to as the SCOPE dataset). This dataset consists of 167 cases generated by randomly assigning values to the input parameters of the model (the same way as described in Section 2.2). For each case, the TOC spectra of total upwelling radiance and SIF radiance with different sensor spectral configurations were simulated. The corresponding spectra of the incident irradiance were also provided. Ten SRs (ranging from 0.1 nm to 1 nm with an increment of 0.1 nm) and eleven SNRs (ranging from 100 to 1000 with a regular logarithmic interval of 0.1 with base 10) were considered. The SCOPE model was coupled with the MODTRAN (version 5.2.1) model to simulate noise-free spectra with SSI of 1 cm^{-1}. Then the spectra were convolved by Gaussian functions and contaminated by random white Gaussian noise using the method by Damm et al. (2011) to simulate the spectra for any combinations of given SR and SNR. The SSIs of the spectra were set to be half of the corresponding SR values, and nadir viewing angle was used for the simulations. This dataset was generated independently of the training datasets.

2.3.2. Dataset simulated for the FLEX/Sentinel-3 Bridge study

A dataset for the FLEX/Sentinel-3 Bridge study (Verhoef et al., 2018) (referred to as the Bridge dataset) was generated by coupling the SCOPE model (version 1.60) with the MODTRAN (version 5.2.1) model. It contains 10 output layers of simulated TOC/TOA/atmospherically corrected spectra of the radiance, the reflectance factor, and SIF radiance for 40 cases comprising various soil, leaf, canopy or atmosphere parameters. The TOC noise-free radiance spectra of canopy (layer 2) and white Lambertian reference panel (layer 3) were used to investigate the SIF reconstruction accuracy for TOC noise-free data. Atmospherically corrected spectra (of TOC irradiance/π and apparent reflectance in layers 5 and 6, respectively) obtained from noisy TOA radiance data were used to explore the potential to reconstruct the SIF spectra for atmospherically corrected spaceborne measurements. The method of the University of Valencia (for compatibility with the end-to-end simulator of the FLEX mission) was adopted for the atmospheric correction to obtain layers 5 and 6 (Verhoef et al., 2018). Errors of the atmospherically corrected data are caused by ignoring surface anisotropy and adjacency effects, the truncation of a geometrical series of TOA radiance, and sensor noise (detailed information can be found in the Supplementary Data). The SIF spectra range from 670 nm to 780 nm, and other simulated spectra cover the range from 500 nm to

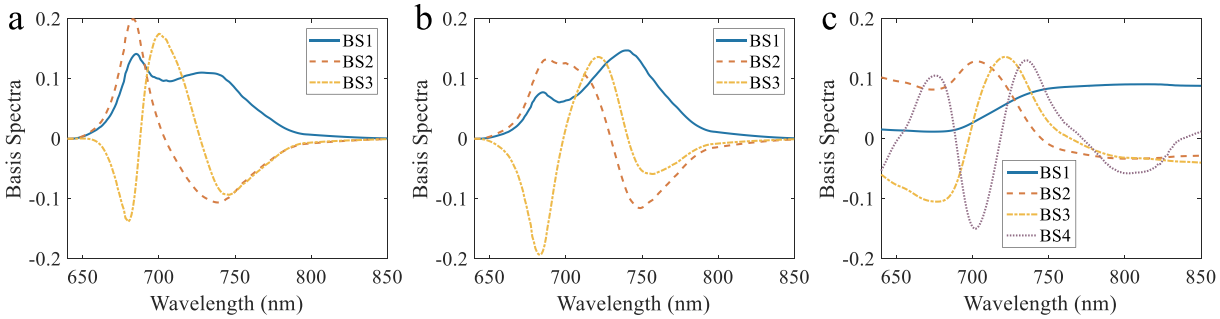

Fig. 3. The first three basis SIF spectra extracted from training dataset I for canopies with low C_{ab} (a) and training dataset II for canopies with medium/high C_{ab} (b); and the first four basis spectra of the reflectance factor extracted from training dataset III for all canopies (c).

780 nm. The SRs, SSIs and SNRs were set to be the same as those projected for the instruments onboard the FLEX and Sentinel-3 satellites (Donlon et al., 2012; ESA, 2015; Coppo et al., 2017). The SRs are higher around O_2-A and O_2-B absorption lines (0.3 nm) than at other wavelengths (0.6–3 nm). Please refer to Verhoef et al. (2018) for more detailed information about this dataset.

2.3.3. Dataset generated by the FluorWPS model

A third test dataset (referred to as the FluorWPS dataset) was generated using the Fluorescence model with Weighted Photon Spread method (FluorWPS model) (Zhao et al., 2016). This model is based on the 3-D Monte Carlo ray-tracing method rather than the four-stream RT theory adopted for 1-D canopies in the SCOPE model. Thus, the potential problems caused by using the same model (SCOPE) to generate both training and test datasets can be avoided. Furthermore, the RT of SIF in a 3-D canopy can be faithfully simulated by FluorWPS, so the capability of the aFSR method to retrieve the SIF spectra for heterogeneous canopies can be evaluated. Therefore, this dataset can serve as a valuable supplement to the other two. Eight cases of explicit vegetative scenes with different canopy structures (1-D, 2-D and 3-D), LAI, C_{ab}, and carotenoid content (C_{ca}) were generated for RT simulation by FluorWPS. The parameters of each case are listed in Table 3 and generated scenes of case 1 (1DLAI0.9C_{ab}40), case 4 (2DLAI0.9C_{ab}40), and case 8 (3DLAI0.9C_{ab}40) are displayed in Fig. 4. For each case, TOC spectra of total upwelling radiance and SIF radiance were calculated at different viewing zenith angles (VZA, 0°–70° with an increment of 5°) in the principal plane. Both forward and backward directions were considered, resulting in a total of 29 viewing angles for each case. Sun zenith and azimuth angles were fixed at 30° and 140°, respectively. Other parameters were set to be consistent among the cases. These parameters include the spectra of incident irradiance and the soil reflectance factor, water content (0.01 g·cm^{-2}), senescent material (0.1), dry matter content (0.005 g·cm^{-2}), leaf inclination distribution type (uniform), and fluorescence quantum yield efficiency for photosystem I (0.004) and photosystem II (0.02). By comparing the results for different cases, the impact of canopy structure, LAI and C_{ab} on the SIF spectrum reconstruction can be investigated. The spectra range from 640 nm to 850 nm, and the SR, SSI and SNR of the spectra were set to 0.3 nm, 0.15 nm and 1000, respectively. This sensor spectral configuration is similar to that of the spectrometer used to obtain the experimental data.

Table 3
Canopy characteristics of the eight cases.

Case	Canopy structure	LAI	C_{ab} (μg·cm^{-2})	C_{ca} (μg·cm^{-2})	Identifier
1	Homogeneous (1-D)	0.9	40	10	1DLAI0.9C_{ab}40
2	Homogeneous (1-D)	2.1	40	10	1DLAI2.1C_{ab}40
3	Homogeneous (1-D)	3.4	40	10	1DLAI3.4C_{ab}40
4	Row (2-D)	0.9	40	10	2DLAI0.9C_{ab}40
5	Row (2-D)	2.1	20	5	2DLAI2.1C_{ab}20
6	Row (2-D)	2.1	40	10	2DLAI2.1C_{ab}40
7	Row (2-D)	2.1	60	15	2DLAI2.1C_{ab}60
8	Heterogeneous (3-D)	0.9	40	10	3DLAI0.9C_{ab}40

2.4. Experimental dataset

The experimental and simulated datasets with the same nominal sensor specification may be quite different due to the high variability inherent to natural environments and the associated difficulties of obtaining accurate and representative experimental data (Zhao et al., 2015b). These uncertain factors may influence the reconstruction of SIF spectrum. Therefore, testing the aFSR method with experimental data is still meaningful and necessary.

Field experiments were conducted in 2016 at the National Precision Agriculture Demonstration Base located north of Beijing, China (40°11′N, 116°27′E). Diurnal variations of the upwelling radiance spectra of winter wheat and reference panel were measured by a customized Ocean Optics QE Pro spectrometer (Ocean Optics, Dunedin, FL, USA) within the spectral range of 645–805 nm and with SR of 0.31 nm, SSI of 0.155 nm, and SNR (maximum possible value) of 1000. Fourteen and seventeen measurements were carried out under clear sky conditions on April 18 (jointing stage) and May 17 (filling stage), 2016,

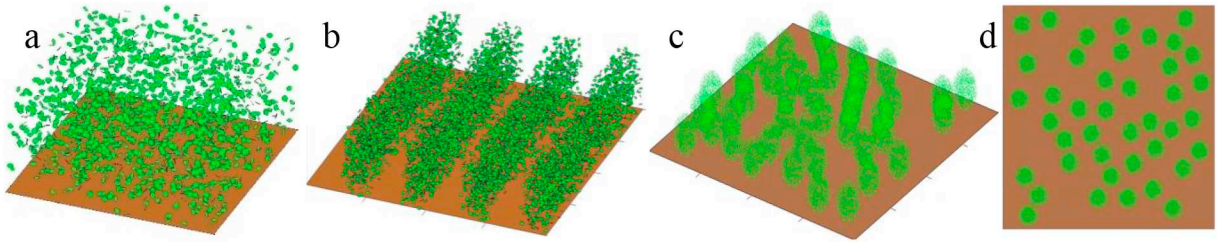

Fig. 4. Generated scenes for cases 1, 4, and 8: a) side view of 1-D canopy (case 1, 1DLAI0.9C_{ab}40), b) side view of 2-D row canopy (case 4, 2DLAI0.9C_{ab}40), c) side view and d) vertical view of 3-D heterogeneous canopy (case 8, 3DLAI0.9C_{ab}40).

Table 4
Summary of the main features of the test datasets.

Dataset	Data type	Spectral resolution (SR)	Spectral sampling interval (SSI)	Signal-to-noise ratio (SNR)	Data format	Number of cases
The SCOPE dataset	Simulation (SCOPE)	Ranging from 0.1 nm to 1 nm with an increment of 0.1 nm	0.5 × SR	Ranging from 100 to 1000 with a regular logarithmic interval of 0.1 with base 10	TOC spectra of upwelling radiance and incident irradiance	167 (by varying the15 most influential SCOPE input parameters)
The Bridge dataset	Simulation (SCOPE & MODTRAN)	Setting to be the same as those of the instruments onboard the FLEX and Sentinel-3 satellites			TOC and atmospherically corrected spectra of upwelling radiance and incident irradiance	40 (by varying 9 surface parameters and 6 atmospheric parameters)
The FluorWPS dataset	Simulation (FluorWPS)	0.3 nm	0.15 nm	1000	TOC spectra of upwelling radiance and incident irradiance	8 (by varying canopy structure, LAI, C_{ab}, and C_{ca}) × 29 (by varying VZA)
Experimental dataset	Field measurement (winter wheat)	0.31 nm	0.155 nm	1000 (maximum possible value[a])	TOC spectra of upwelling radiance and incident irradiance	14 (measured on April 18, 2016) + 17 (measured on May 17, 2016)

[a] https://oceanoptics.com/glossary/#s-n.

respectively. More detailed information about this dataset can be found in Liu et al. (2017).

A summary of the main features of the simulated and experimental datasets is given in Table 4.

2.5. Accuracy assessment of the reconstructed SIF spectrum

For simulated test datasets, the reconstructed SIF spectra can be compared with the true simulated spectra to evaluate the reconstruction accuracies. The relative root-mean-square error (RRMSE) is a scale-independent indicator of the accuracy of reconstructed SIF spectra and is used for later comparisons. It is calculated by Eq. (7):

$$RRMSE = \sqrt{\frac{\sum_{j=1}^{n}\left(\frac{F_{rec,i}(\lambda)-F_{t,i}(\lambda)}{F_{t,i}(\lambda)}\right)^2}{n}} \times 100\% \quad (7)$$

where $F_{rec,i}(\lambda)$ and $F_{t,i}(\lambda)$ are the retrieved and true SIF radiance of case i at wavelength λ, respectively, j is the index for different cases or wavelengths and n is the number of cases. The average of the RRMSEs of different cases is also calculated to measure the overall reconstruction accuracy for both different cases and different wavelengths.

Since RRMSE cannot reveal whether the algorithms tend to overestimate or underestimate SIF radiance, average relative errors (AREs) are adopted and calculated by Eq. (8):

$$ARE = \frac{\sum_{i=1}^{n}\frac{F_{rec,i}(\lambda)-F_{t,i}(\lambda)}{F_{t,i}(\lambda)}}{n} \times 100\% \quad (8)$$

The absolute relative errors and the average absolute relative errors (AARE, Eq. (9)) of the spectrally-integrated SIF are also calculated since the spectrally-integrated SIF is valuable for the estimation of photosynthesis rates and is one of the planned L2 products of the FLEX mission.

$$AARE = \frac{\sum_{i=1}^{n}\left|\frac{F_{rec,i}^{int}-F_{t,i}^{int}}{F_{t,i}^{int}}\right|}{n} \times 100\% \quad (9)$$

where $F_{rec,\ i}^{\ int}$ and $F_{t,\ i}^{\ int}$ are the retrieved and true spectrally-integrated values of the SIF spectra for case i, respectively. The FLEX mission aims to retrieve the spectrally-integrated SIF with the absolute relative error < 10% (ESA, 2015), which is therefore adopted as a criterion of tolerable reconstruction accuracy for later analyses.

For the experimental dataset, absolute reconstruction accuracy cannot be directly calculated since the actual SIF spectra are unknown. However, it is feasible to compare the SIF spectra reconstructed by four different methods against each other to document their relative differences. By reference to the strategy adopted by the radiation transfer model intercomparison exercise (Widlowski et al., 2013), where the true value of the target quantity is also unknown, we compared the SIF spectra reconstructed by each method with the reference spectra calculated as the average of the SIF spectra reconstructed by the other three methods. To quantify the difference between the SIF spectra reconstructed through each method and the reference SIF spectra, the coefficient of determination (R^2), root-mean-square error (RMSE), standard deviation (STD), and bias (mean error) between them were calculated.

3. Results

In this section, the accuracy of the aFSR method is evaluated by four test datasets. The results of the FSR, F-SFM, and SpecFit methods are also provided for comparison.

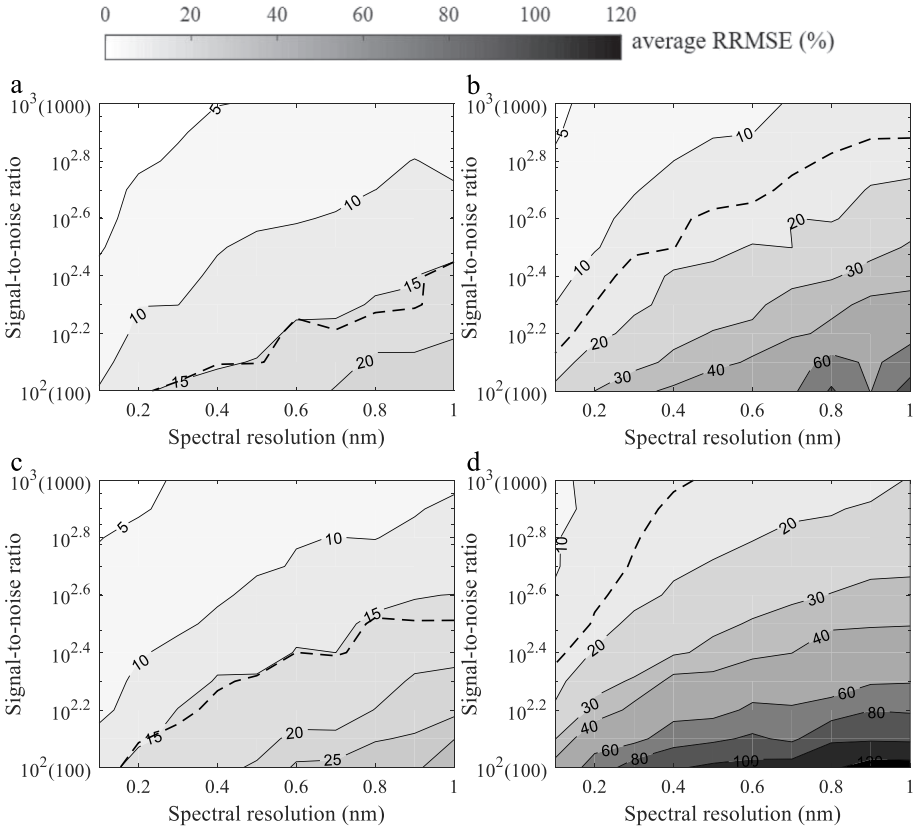

Fig. 5. Contours of the average RRMSE of the SIF spectra reconstructed by aFSR (a), FSR (b), F-SFM (c), and SpecFit (d) as a function of spectral resolution (SR) and signal-to-noise ratio (SNR) (solid lines). The dashed lines show the contours of 10% AARE of the spectrally-integrated SIF. The axes for SNR are plotted on logarithmic scale.

3.1. Results for the SCOPE dataset

Contours of the average RRMSE of the reconstructed SIF spectra (average of the RRMSE for all cases) as a function of SR and SNR (in logarithmic scale) are displayed as solid lines in Fig. 5. The dashed lines added to the contour maps show the contours of AARE of the spectrally-integrated value of reconstructed SIF spectra equal to 10%. The regions to the upper left of the dashed lines correspond to AAREs that are < 10%, which means that the accuracy standard set by the FLEX mission is achieved. Among the four method, the aFSR method can achieve this accuracy standard with minimum requirement of spectral resolving power and SNR (e.g., SR ≤ 0.6 nm and SNR ≥ 200). The reconstruction accuracy of aFSR deteriorates when both spectral resolving power (negatively related to SR) and SNR, or either of them, decrease. Similar trend is also found for the FSR, F-SFM, and SpecFit methods. For most combinations of SR and SNR, the aFSR method provides the highest reconstruction accuracies. For instance, for the data with SR and SNR similar to those of the FluorWPS and experimental datasets (SR = 0.3 nm, SNR = 1000), the average RRMSE is 4.1% for the aFSR method and 7.1%, 5.1%, and 12.5% for the FSR, F-SFM, and SpecFit methods, respectively.

The numbers of basis spectra of SIF and reflectance factor (N_fs and N_rs) used by the aFSR, FSR, and F-SFM methods for data with different SRs and SNRs are presented in Table 5, since they partially determine the accuracies of these methods. The cells with AARE of the spectrally-integrated SIF < 10% are highlighted in yellow. Due to limited space, we only present N_fs and N_rs for data with SNR higher than 300 (which is more widely adopted by field spectrometers). It is found that the number of basis spectra used by those methods generally increase with the increase of spectral resolving power and SNR. For data with the same SR and SNR, N_f used for aFSR is always larger than or equal to that for FSR and F-SFM. N_rs for aFSR are average values because the N_rs determined for different cases with the same SR and SNR can be different. The determination of these N_fs and N_rs is discussed in Sections 4.1 and 4.2.

3.2. Results for the Bridge dataset

RRMSEs of the SIF spectra reconstructed for TOC noise-free data and atmospherically corrected data in the Bridge dataset are shown in Fig. 6a and b, respectively. For the TOC noise-free data, the aFSR method generally provides the highest reconstruction accuracy with RRMSEs < 4.8% for all wavelengths (Fig. 6a) and with relative errors of the spectrally-integrated SIF < 10% for all cases. Higher reconstruction accuracies are observed at around O_2-A and O_2-B absorption lines, where the most important information for the reconstruction is provided (Fig. 6a). The FSR, F-SFM and SpecFit methods can also reconstruct SIF spectrum with relatively high accuracy (RRMSEs < 10% for most wavelengths), but the aFSR method provides the highest reconstruction accuracy at wavelengths longer than 709 nm (Fig. 6a).

When the effect of atmospheric correction is considered, the range of RRMSE for aFSR increases from 1.2%–4.8% (Fig. 6a) to 7.5%–14.4% (Fig. 6b). Higher RRMSEs are observed around the O_2-A and O_2-B absorption lines, where larger atmospheric correction errors occur (see the Supplementary data). At all wavelengths, the highest reconstruction accuracies are provided by aFSR (Fig. 6b). Moreover, the aFSR method achieves the accuracy with the absolute relative error of the spectrally-integrated SIF < 10% for more cases than the other three methods: 82.5% compared with 37.5%, 60%, and 12.5% for FSR, F-SFM, and SpecFit, respectively. The results achieved are based on the typical equation which describes the TOC radiance as additive combination of reflected and fluorescence radiance. Improved results may be obtained by using the coupling process suggested in (Sabater et al., 2017), which needs further investigation.

Table 5
The numbers of basis SIF spectra (N_fs) and the average numbers of basis spectra of the reflectance factor (average N_rs) used for aFSR, N_fs used for FSR, and the combinations of N_f and N_r used for F-SFM for data with different SRs and SNRs in the SCOPE dataset. The cells with AARE of the spectrally-integrated SIF < 10% are highlighted in yellow.

Method	SNR \ SR (nm)	0.1	0.2	0.3	0.4	0.5	0.6	0.7	0.8	0.9	1
aFSR	316	3, 10.2[a]	2, 9.6	2, 9.4	2, 9.2	2,9.1	2, 8.9	2, 8.9	2, 8.7	2, 8.6	2, 8.6
	398	3, 10.8	3, 10.1	2, 9.6	2, 9.5	2, 9.5	2, 9.3	2, 9.2	2, 9.1	2, 8.9	2, 9.0
	501	3, 11.4	3, 10.4	3, 10.1	2, 10.0	2, 9.8	2, 9.7	2, 9.5	2, 9.4	2, 9.3	2, 9.4
	631	3, 12.3	3, 11.2	3, 10.7	3, 10.2	2, 10.3	2, 10.1	2, 10.1	2, 9.9	2, 9.8	2, 9.7
	794	4, 12.6	3, 11.9	3, 11.1	3, 10.9	3, 10.5	2, 10.8	2, 10.5	2, 10.4	2, 10.2	2, 10.2
	1000	4, 13.2	3, 12.5	3, 12.1	3, 11.4	3, 11.1	3, 10.9	3, 10.7	2, 11.1	3, 10.4	2, 10.7
FSR	316	2[b]	2	2	2	2	2	2	1	1	2
	398	2	2	2	2	2	2	2	2	1	2
	501	2	2	2	2	2	2	2	2	1	2
	631	3	2	2	2	2	2	2	2	2	2
	794	3	2	2	2	2	2	2	2	2	2
	1000	3	2	2	2	2	2	2	2	2	2
F-SFM	316	2, 8[c]	2, 9	2, 11	2, 9	2, 9	2, 8	2, 9	2, 7	1, 9	1, 9
	398	2, 24	2, 9	2, 24	2, 11	2, 9	2, 8	1, 9	2, 9	2, 9	1, 9
	501	2, 24	2, 24	2, 11	2, 16	2, 9	2, 9	2, 9	2, 8	2, 9	2, 9
	631	2, 24	2, 15	2, 15	2, 13	2, 11	2, 9	2, 9	2, 9	2, 11	2, 8
	794	2, 24	2, 24	2, 23	2, 24	2, 11	2, 11	2, 13	2, 9	2, 9	2, 11
	1000	2, 24	2, 24	2, 24	2, 24	2, 11	2, 21	2, 13	2, 21	2, 11	2, 20

[a] N_f, average N_r; [b] N_f; [c] N_f, N_r.

3.3. Results for the FluorWPS dataset

The RRMSEs of the SIF spectra reconstructed through aFSR as well as the FSR, F-SFM, and SpecFit methods under different viewing angles in the principal plane are shown in Fig. 7 for each case. The RRMSE distributions for different sensor spectral characteristics are similar. Due to limited space, we only present the results for data with SR and SNR of 0.3 nm and 1000, respectively.

It can be seen that the highest reconstruction accuracy is generally provided by aFSR. Except for the hot spot direction, an accuracy of 10% absolute relative error of the spectrally-integrated value of reconstructed SIF spectrum can always be achieved by the aFSR method, while it is achieved by the FSR, F-SFM and SpecFit methods for 84%, 94%, and 66% of the cases, respectively. Compared with the other methods, the accuracy of aFSR is less affected by viewing angles, which implies that the aFSR method can be applied to data observed at oblique viewing angles. Local maxima of RRMSE are frequently observed at the hot spot direction (30°) for aFSR as well as the other three methods, which is caused by the anisotropy of surface reflectance. At the hot spot direction, the bi-directional reflectance factor (BRF) is significantly higher than the hemispheric-directional reflectance factor (HDRF). Hence the shorter photon path corresponding to solar incident and directly reflected sunrays receives more weight, and in that case atmospheric absorption lines appear to be shallower compared with the cases where BRF and HDRF are similar (Cogliati et al., 2015b; Verhoef et al., 2018). Consequently, the shallower absorption line may be misinterpreted as an in-filling effect due to SIF and lead to an overestimation of SIF (as shown in Fig. 8). It should be noted that the highest reconstruction accuracy is still generally provided by the aFSR method at the hot spot direction.

Fig. 8 shows the contours of average relative error (ARE) of retrieved SIF radiance as a function of VZA and wavelength. Absolute AREs of the aFSR method are generally < 10% at wavelengths longer than 685 nm, which are usually lower than those by the FSR and SpecFit methods. When the viewing angle deviates from the hot spot direction, the error patterns for all the methods change around 690 nm, which may be explained by the model difference between FluorWPS and the SCOPE model and is explained in Section 4.2.

The impact of canopy structure on the reconstruction accuracy of the SIF spectrum can be evaluated by analyzing two groups' results. Each group consists of cases with different canopy structures but the same LAI and C_{ab}: 1) case 1 (1DLAI0.9C_{ab}40), case 4 (2DLAI0.9C_{ab}40), and case 8 (3DLAI0.9C_{ab}40); 2) case 2 (1DLAI2.1C_{ab}40) and case 6 (2DLAI2.1C_{ab}40). The averages of the RRMSEs at different VZAs are given in Table 6 for all cases in the two groups. Since no systematic influence of pigment contents (C_{ab} and C_{ca}) and LAI on the

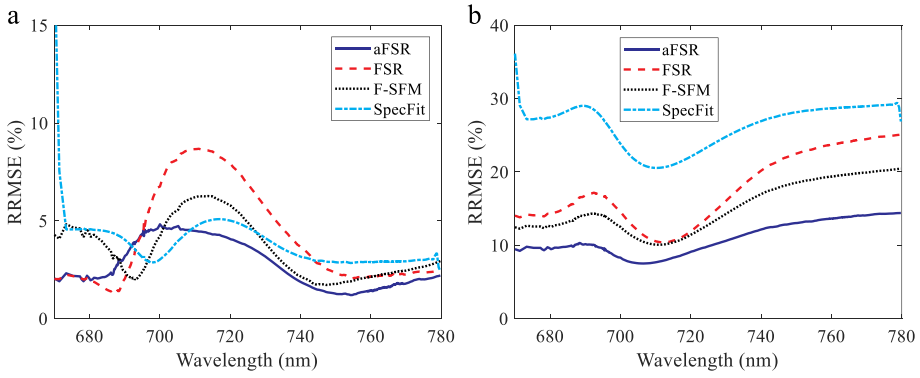

Fig. 6. RRMSEs of the SIF spectra reconstructed by aFSR (blue solid lines), FSR (red dashed lines), F-SFM (black dotted lines), and SpecFit (cyan dash-dot lines) for simulated TOC noise-free data (a) and atmospherically corrected data (b) at different wavelengths. (For interpretation of the references to colour in this figure legend, the reader is referred to the web version of this article.)

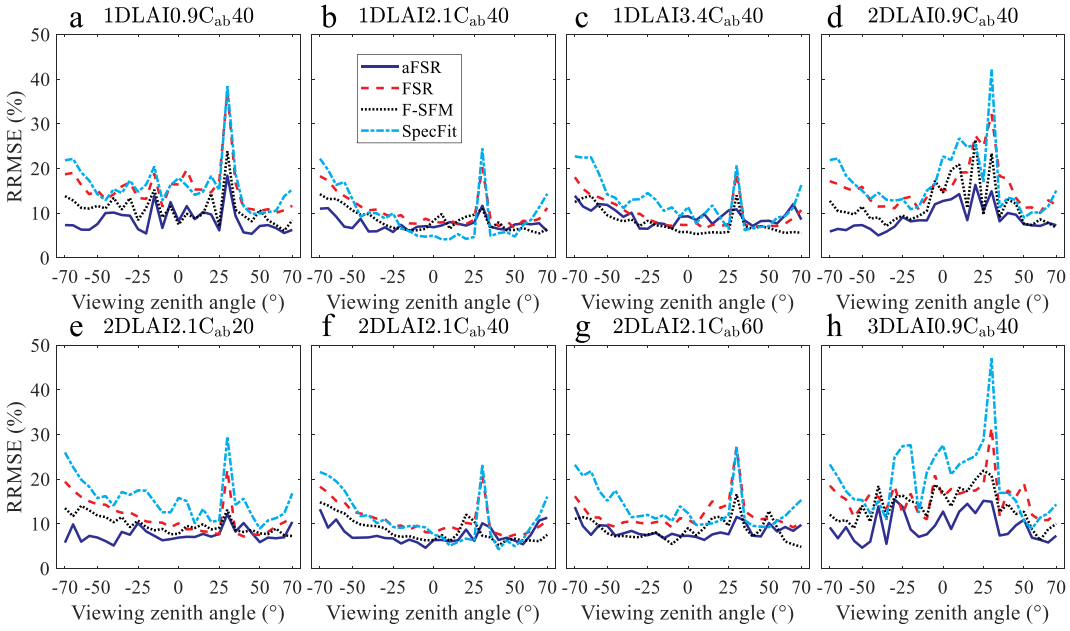

Fig. 7. Changes of RRMSEs of the SIF spectra reconstructed through aFSR (blue solid lines), FSR (red dashed lines), F-SFM (black dotted lines), and SpecFit (cyan dash-dot lines) for the eight cases with respect to viewing zenith angle (VZA). The negative VZAs correspond to forward directions while the positive ones correspond to backward directions. (For interpretation of the references to colour in this figure legend, the reader is referred to the web version of this article.)

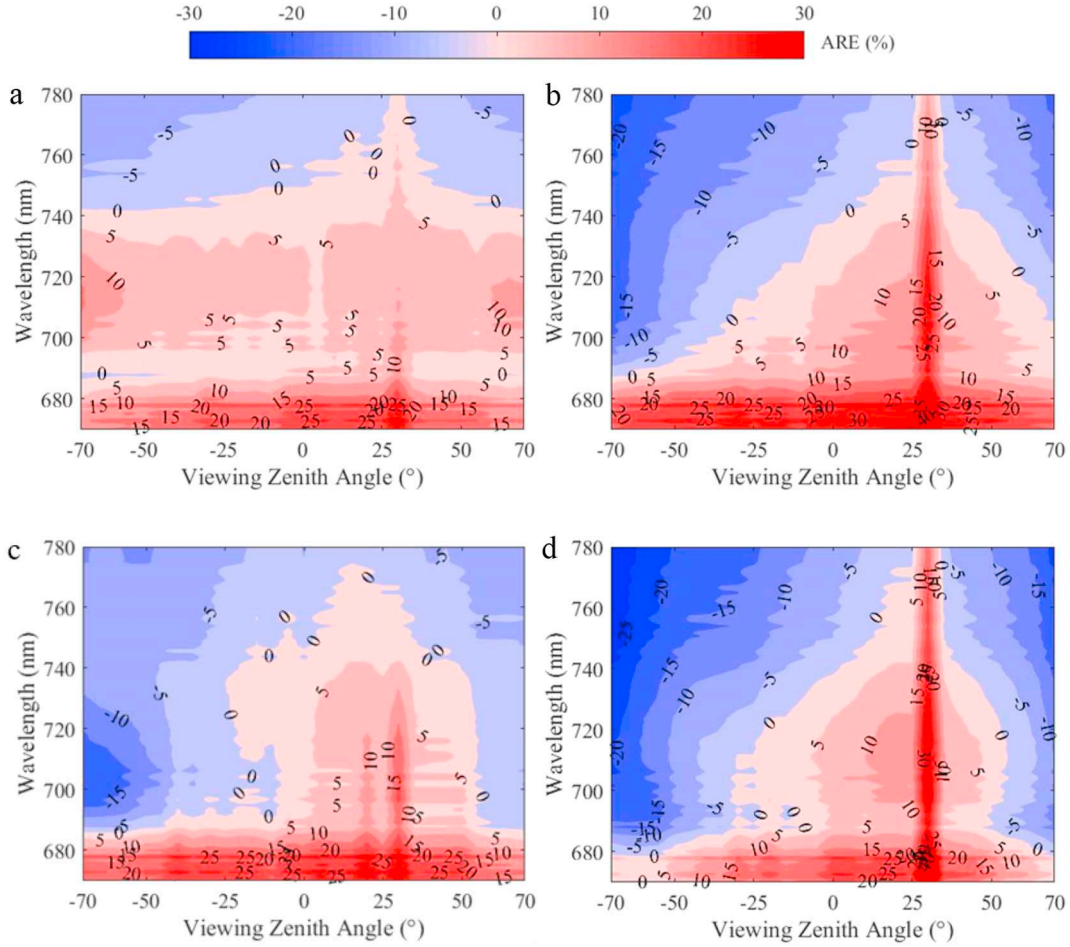

Fig. 8. Contours of the average relative error of the SIF spectra reconstructed through aFSR (a), FSR (b), F-SFM (c), and SpecFit (d) as a function of VZA and wavelength. The negative zenith angles correspond to forward direction while the positive ones correspond to backward direction.

Table 6
Average of the RRMSEs for different VZAs for cases with different canopy structures.

Method	Group 1			Group 2	
	1DLAI0.9C_{ab}40	2DLAI0.9C_{ab}40	3DLAI0.9C_{ab}40	1DLAI2.1C_{ab}40	2DLAI2.1C_{ab}40
aFSR	8.46% (8.10%)	8.92% (8.71%)	9.56% (9.37%)	7.53% (7.38%)	7.58% (7.49%)
FSR	15.36%[a] (14.58%[b])	15.70% (15.11%)	15.86% (15.29%)	10.28% (9.93%)	10.77% (10.41%)
F-SFM	10.87% (10.40%)	11.78% (11.37%)	13.93% (13.69%)	8.45% (8.36%)	8.52% (8.56%)
SpecFit	16.22% (15.43%)	16.86% (15.96%)	19.77% (18.80%)	9.42% (8.88%)	10.83% (10.39%)

[a] Average of RRMSEs for all VZAs.
[b] Average of RRMSEs for all VZAs except 30° (corresponding to the hot spot direction).

reconstruction accuracy of the SIF spectrum is observed, the comparison results of average RRMSE for these factors are not presented here.

With the increase of canopy heterogeneity (from 1-D to 3-D), the maximum variations of the average RRMSEs with canopy structure in the two groups are > 3% for F-SFM and SpecFit. However, the maximum variations for aFSR and FSR are relatively lower: 1.10% and 0.50%, respectively. Besides, the aFSR method provides higher accuracies than the FSR method, demonstrating that the aFSR method can consistently provide high accuracies for canopies with different 3-D structures.

3.4. Results for the experimental dataset

Fig. 9 shows the diurnal variations of the SIF spectrum reconstructed by aFSR and the other three methods for the field experimental dataset obtained on April 18 and May 17, 2016. Shapes and diurnal variation trends of the SIF spectrum reconstructed by aFSR show high consistency with those by the other three methods. The red and far-red SIF peaks are successfully reconstructed and the shapes of the reconstructed spectra are reasonable according to other early studies (Meroni et al., 2009). Furthermore, the magnitude of the reconstructed SIF spectra at both O_2-A and O_2-B bands agree well with those reported in the other studies (Liu et al., 2013; Cogliati et al., 2015a; Rossini et al., 2016). It is also observed that the SIF radiance generally increases in the morning and decreases in the afternoon, which agrees with the diurnal variation of incident irradiance and is consistent with earlier studies (Liu et al., 2013; Zhao et al., 2014). At 12:30 pm on April 18, and at 11:03 am on May 17, the reconstructed SIF spectra are abnormal in that they are not in accord with the diurnal variation trend of the reconstructed spectra, which may be caused by uncertain experimental factors.

The SIF spectra reconstructed by each method were compared with

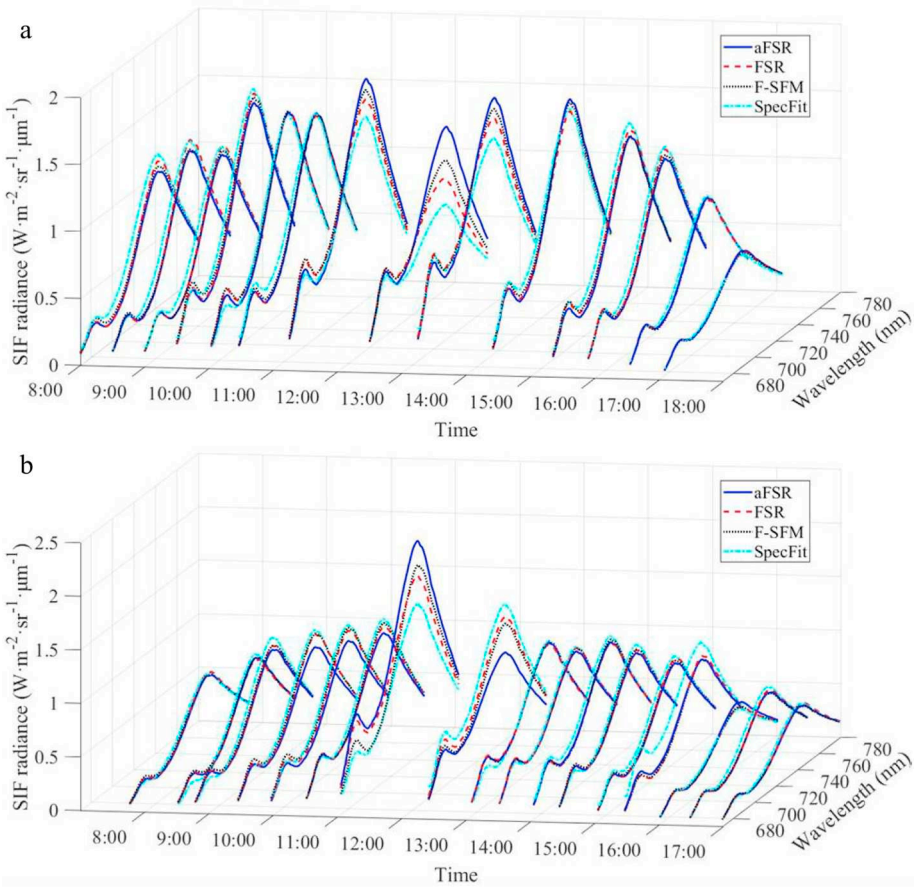

Fig. 9. Diurnal variations of the SIF spectra reconstructed through aFSR (blue solid lines), FSR (red dashed lines), F-SFM (black dotted lines), and SpecFit (cyan dash-dot lines), for measurements on April 18, 2016 (a) and May17, 2016 (b) at the National Precision Agriculture Demonstration Base located north of Beijing, China. The reconstructed SIF spectra are abnormal at 12:30 pm on April 18, and at 11:03 am on May 17. (For interpretation of the references to colour in this figure legend, the reader is referred to the web version of this article.)

Table 7
Statistics obtained by comparing the SIF spectra reconstructed through one method with the reference SIF spectra.

	April 18, 2016				May17, 2016			
	aFSR	FSR	F-SFM	SpecFit	aFSR	FSR	F-SFM	SpecFit
R^2	0.9605	0.9933	0.9947	0.9397	0.9327	0.9907	0.9896	0.9196
RMSE ($W{\cdot}m^{-2}{\cdot}sr^{-1}{\cdot}\mu m^{-1}$)	0.0799	0.0319	0.0284	0.0951	0.0867	0.0309	0.0328	0.959
STD ($W{\cdot}m^{-2}{\cdot}sr^{-1}{\cdot}\mu m^{-1}$)	0.0799	0.0313	0.0281	0.0951	0.0843	0.0308	0.0326	0.0921
Bias ($W{\cdot}m^{-2}{\cdot}sr^{-1}{\cdot}\mu m^{-1}$)	−0.0010	−0.0064	0.0042	0.0032	−0.0202	−0.0035	−0.0029	0.0266

the reference spectra which were calculated as the average of the SIF spectra reconstructed through the other three methods. The statistics R^2, RMSE, STD, and bias were calculated and listed in Table 7. It is shown that the SIF spectra reconstructed by aFSR are closely in agreement with the reference spectra (with R^2 higher than 0.93 and RMSE lower than 0.09 $W{\cdot}m^{-2}{\cdot}sr^{-1}{\cdot}\mu m^{-1}$). The close agreement implies that aFSR is also applicable to actual experimental data, since the FSR, F-SFM, and SpecFit methods have been validated by other experimental datasets before. It should be noted that the statistics do not reflect the absolute reconstruction accuracy since the true SIF spectra is unknown.

4. Discussions

4.1. Determination of the numbers of basis spectra used for the aFSR method

The number of basis spectra used can affect reconstruction accuracy. Theoretically, more basis spectra can better represent the spectra of SIF or the reflectance factor. However, if more basis spectra are used, more coefficients need to be determined. Since the information content provided by given remote sensing data is limited, the more coefficients need to be determined, the less information is allocated to each coefficient. Consequently, the coefficients may not be accurately retrieved, and reconstruction error occurs.

By referring to Table 5, N_f was determined to be 3 for the FluorWPS dataset and the TOC noise-free data in the Bridge dataset. For the atmospherically corrected data in the Bridge dataset and the experimental dataset, the uncertainty of the data is higher than that of simulated TOC data with the same nominal sensor characteristics. Therefore, a relatively conservative strategy was used for the determination of N_f for the experimental dataset: using 2 basis spectra. The determined N_fs and the average N_rs for the Bridge, FluorWPS, and experimental datasets are presented in Table 8.

It is observed in Tables 5 and 8 that N_r is always larger than N_f. Since reflected radiance dominates the total TOC radiance (generally contributes to larger than 75% of the total TOC radiance except for wavelengths around the O_2-B absorption line), small errors in the estimation of the reflectance factor can lead to large deviation of the estimated reflected radiance and consequently the retrieved SIF radiance. So, more basis spectra of the reflectance factor are used to accurately fit the spectrum of the reflectance factor. The N_r chosen by BIC is generally different from the N_r determined by the best N_f and N_r determination method (to be explained in Section 4.2). However, the accuracies of the SIF spectrum reconstructed with N_r determined by these two methods are quite close (see Supplementary data), indicating that BIC can be used as a proper method to determine N_r for the aFSR method.

Table 8
N_fs and average N_rs used by the aFSR method for the Bridge, FluorWPS, and experimental datasets.

Method	The Bridge dataset (TOC noise-free)[a]	The Bridge dataset (atmospherically corrected)[b]	The FluorWPS dataset[c]	The experimental dataset[d]
aFSR	3, 16.1[e]	2, 10.1	3, 27.8	2, 29.4

[a] SR is set to be the same as those of the instruments onboard the FLEX and Sentinel-3 satellites.
[b] SR and SNR are set to be the same as those of the instruments onboard the FLEX and Sentinel-3 satellites.
[c] SR and SNR are set as 0.3 nm and 1000, respectively.
[d] SR and SNR are 0.31 nm and 1000, respectively.
[e] The number of basis SIF spectra (N_f) and the average number of basis spectra of the reflectance factor (average N_r).

4.2. Comparison with the other three SIF spectrum reconstruction methods

The aFSR method is similar to the FSR and F-SFM methods in that they all exploit training datasets for feature extraction of the spectra of SIF and the reflectance factor (the aFSR and F-SFM methods) or the SIF spectrum (the FSR method). The accuracy of these methods depends on the representativeness of the training datasets. For instance, by comparing the SIF spectrum reconstruction accuracies for data with the same viewing direction (VZA = 0°) and spectral characteristics (SR = 0.3 nm and SNR = 1000) in the SCOPE and FluorWPS datasets, it is found that accuracies of the aFSR, FSR, and F-SFM methods for the FluorWPS dataset (Fig. 7) are generally lower than those achieved for the SCOPE dataset (Fig. 5): for data in the FluorWPS dataset, the average RRMSEs for 1-D canopies are 8.1%, 10.6%, and 7.2% for the aFSR, FSR, and F-SFM methods, respectively; for data in the SCOPE dataset, the average RRMSEs for those methods are 4.1%, 7.1%, and 5.1%, respectively. However, for the SpecFit method which does not exploit training datasets, the average RRMSE for 1-D canopies in the FluorWPS dataset (11.4%) is similar to that for data in the SCOPE dataset (12.5%). The degradation of the accuracy of the aFSR, FSR, and F-SFM method and the pattern changes of ARE for the retrieved SIF radiance around 690 nm (Fig. 8) can be explained by the difference between the SCOPE and FluorWPS models. According to Zhao et al. (2016), the SIF radiance at wavelengths longer than 690 nm simulated by the FluorWPS model is systematically higher than that simulated by the SCOPE model, while the SIF radiance at wavelengths shorter than 690 nm simulated by the two models agrees better. The deviation of the two models introduces errors when fitting the FluorWPS-generated SIF spectra based on the training dataset simulated by SCOPE. The difference of the SIF spectra simulated by the two models is mainly caused by the different formulations used to calculate the scattering contributions to SIF (Zhao et al., 2016). Theoretically, the SIF spectra simulated by the FluorWPS model should be more accurate. But the training datasets are still simulated by the SCOPE model since simulating thousands of cases by the FluorWPS model is very time consuming. Now we are working to improve the efficiency of the FluorWPS model to make it applicable to such large numbers of simulations.

While the FSR and F-SFM methods mainly exploit information around discrete solar or telluric absorption lines to determine the coefficients of the basis SIF spectra, the aFSR method uses all available bands in the SIF emission region. Since more information is used by aFSR, the reconstruction is more robust and accurate. Also, more coefficients can be reliably determined. For the same data, N_f for the aFSR method is usually larger than or at least equal to that for the FSR and F-SFM methods. For instance, four basis SIF spectra can be used by

Table 9
Spectral and spatial specifications of satellite instruments that have the potential to be used to reconstruct the full SIF spectrum.

Instrument/satellite	GOME-2/Metop	SCIAMACHY/ENVISAT	TROPOMI/Sentinel-5	FLORIS/FLEX
Spectral coverage	240–790 nm (640–790 nm[a])	240–1750 nm, 1940–2040 nm, 2265–2380 nm (640–850 nm)	270–495 nm, 675–775 nm, 2305–2385 nm (675–775 nm)	500–780 nm (640–780 nm)
Spectral resolution at 640–850 nm	0.48 nm	0.48–0.54 nm	0.34–0.35 nm	0.3–3 nm
Spatial resolution	40 × 80 km^2[b]	30 × 30–240 km^2[c]	3.5 × 7 km^2	300 × 300 m^2
Signal-to-noise ratio	> 1000	> 1000	200–600	115–1015
Reference	Joiner et al., 2013	Joiner et al., 2012	Guanter et al., 2015	ESA, 2015

[a] The spectral range can be exploited for full SIF spectrum reconstruction.
[b] GOME-2 on MetOp-A has been operating in a reduced-swath mode with a pixel size of 40 × 40 km^2 since 15 July 2013.
[c] The spatial resolution varies along the orbit.

aFSR to reconstruct the SIF spectra for data with SR = 0.1 nm and SNR ≥ 794 in the SCOPE dataset, while only 2 or 3 basis spectra can be used by the FSR and F-SFM methods (Table 5).

In this study, the N_fs and N_rs used for the FSR and F-SFM methods are determined by the best N_f and N_r determination method: for data with each sensor spectral configuration in every simulated dataset, the SIF spectra were reconstructed by employing different numbers of basis spectra, then the N_fs or the combinations of N_f and N_r that provide the highest reconstruction accuracy with respect to the true SIF spectra were selected; for experimental datasets, the numbers of basis spectra that provide reconstrcted SIF spectra with the most reasonable shapes and magnitudes according to earlier studies were selected, which is rather subjective. The determination of N_r is more difficult than that of N_f because N_r has a larger range of variation and its relationship to sensor spectral characteristics is less evident: as shown in Table 5, the best N_r for F-SFM ranges from 7 to 24 and its relationship to SR and SNR is not monotonic. Therefore, it is difficult to determine a proper N_r simply based on prior knowledge. When N_r is not properly determined, the accuracy of the F-SFM method is limited. In contrast, this problem is avoided by the aFSR method by adopting BIC to self-adaptively select proper N_r. Even though the FSR and F-SFM methods use the best N_fs and N_rs while the aFSR method self-adaptively selects N_r, the accuracy of aFSR is generally higher than the FSR and F-SFM methods. Therefore, the aFSR method is more appropriate to be applied to actual experimental data.

The aFSR and SpecFit methods both apply spectral fitting over the full spectral range of SIF emission. Thus, they have the advantage of employing all available information. Unlike aFSR, SpecFit does not require training datasets. Therefore, the problem of representativeness of training datasets does not exist. However, the function used by SpecFit (the sum of two Pseudo-Voigt functions) to approximate the SIF spectrum was determined based on TOC noise-free data in an earlier version of the Bridge dataset. This function may not be optimal for the description of SIF spectra in other datasets. As can be seen in Section 3, the SpecFit method can achieve high accuracy (RRMSE generally < 5.1%) for TOC noise-free data in the Bridge dataset, but it is generally the least accurate for other simulated datasets. Besides, SpecFit needs to determine 9 coefficients of the SIF spectrum while only 2–4 are needed for the aFSR method. Accurately determining these 9 coefficients is quite difficult. Furthermore, while the aFSR method adopts the linear least squares (LLS) approach to reconstruct the SIF spectrum (Eq. (3)), a non-linear least squares (NLLS) approach has to be used for the SpecFit method. Normally, the NLLS approach faces more difficulties than the LLS approach: 1) it may be trapped in local minima; and 2) a time-consuming iterative process has to be adopted. Therefore, the aFSR method is generally more accurate and efficient than the SpecFit method.

4.3. Prospect of reconstructing the SIF spectrum from spaceborne measurements

Reconstruction of the SIF spectrum from spaceborne measurements can provide a synoptic perspective of the surface targets. Four spaceborne sensors cover the major spectral range of SIF emission with a relatively high SR, and may have the potential to be used for SIF spectrum reconstruction are listed in Table 9.

Among the four instruments listed in Table 9, GOME-2, SCIAMACHY and TROPOMI are intended for atmospheric chemistry observations, and SIF is a serendipitous by-product of the missions. Although only SIF at individual wavelengths or in parts of its emission range were retrieved for these instruments in former studies, theoretically it is feasible that the measurements of these instruments can be exploited for SIF spectrum reconstruction. However, due to their low spatial resolution, the heterogeneity at canopy or stand scales cannot be accurately characterized with these instruments (Verrelst et al., 2016). By contrast, FLORIS adopts a finer and ecologically relevant spatial resolution of 300 m, and thus can capture the scale of individual agricultural and forestry management units (ESA, 2015). Moreover, the FLEX mission will fly in tandem with Sentinel-3 to exploit the synergy among the sensors on board both satellites. The information provided by Sentinel-3 (e.g., the atmospheric status) can also benefit SIF spectrum reconstruction from space.

5. Conclusions

In this paper, we proposed the novel aFSR method to reconstruct the full SIF spectrum and evaluated it with simulated and experimental datasets by a comprehensive comparison with three other existing methods: FSR, F-SFM, and SpecFit. The impacts of SR, SNR, atmospheric correction, canopy structure, leaf biochemical parameters and directional effects on the SIF spectrum reconstruction accuracies were considered. Results showed that while all methods could achieve the accuracy standard set by the FLEX mission (AARE of spectrally-integrated SIF < 10%) when spectral resolving power and SNR are high (e.g., SR ≤ 0.3 nm and SNR ≥ 700), aFSR generally provided the highest reconstruction accuracy. The aFSR method was also more robust than other methods as it was less affected by atmospheric correction, directional effect, and canopy heterogeneity. As to the results of experimental dataset, the SIF spectra reconstructed by aFSR agreed well with literature in terms of shape, magnitude and diurnal variation and were in close agreement with the other methods: the R^2 and the RMSE between the reconstruction results of aFSR and the reference spectra calculated as the average of the SIF spectra reconstructed through the other three methods were higher than 0.93 and lower than 0.09 $W{\cdot}m^{-2}{\cdot}sr^{-1}{\cdot}\mu m^{-1}$, respectively.

Research topics for the near future include: 1) reconstruction of the SIF spectrum with spaceborne measurements and analysis of the impact of atmospheric effect on reconstruction accuracy; 2) more systematic evaluation of the impact of directional effects and canopy structures on SIF spectrum reconstruction; and 3) generation of more representative training datasets.

Acknowledgments

This work was supported by the National Natural Science Foundation of China (Projects 41371325 and Grant No. 41771382). The Bridge dataset has been kindly provided by team members involved in the FLEX Bridge Study developed under the ESA ESTEC Contract No. 4000112341/14/NL/FF/gp. Thanks go to M. Celesti for helping to process the Bridge dataset. The authors are grateful to the anonymous reviewers for their constructive comments and suggestions for this improved manuscript.

Declarations of interest

None.

Appendix A. Supplementary data

Supplementary data to this article can be found online at https://doi.org/10.1016/j.rse.2018.10.021.

References

Ač, A., Malenovský, Z., Olejníčková, J., Gallé, A., Rascher, U., Mohammed, G., 2015. Meta-analysis assessing potential of steady-state chlorophyll fluorescence for remote sensing detection of plant water, temperature and nitrogen stress. Remote Sens. Environ. 168, 420–436.

Agati, G., Mazzinghi, P., di Paola, M.L., Fusi, F., Cecchi, G., 1996. The F685/F730 chlorophyll fluorescence ratio as indicator of chilling stress in plants. J. Plant Physiol. 148, 384–390.

Buschmann, C., 2007. Variability and application of the chlorophyll fluorescence emission ratio red/far-red of leaves. Photosynth. Res. 92, 261–271.

Cogliati, S., Rossini, M., Julitta, T., Meroni, M., Schickling, A., Burkart, A., Pinto, F., Rascher, U., Colombo, R., 2015a. Continuous and long-term measurements of reflectance and sun-induced chlorophyll fluorescence by using novel automated field spectroscopy systems. Remote Sens. Environ. 164, 270–281.

Cogliati, S., Verhoef, W., Kraft, S., Sabater, N., Alonso, L., Vicent, J., Moreno, J., Drusch, M., Colombo, R., 2015b. Retrieval of sun-induced fluorescence using advanced spectral fitting methods. Remote Sens. Environ. 169, 344–357.

Coppo, P., Taiti, A., Pettinato, L., Francois, M., Taccola, M., Drusch, M., 2017. Fluorescence imaging spectrometer (FLORIS) for ESA FLEX mission. Remote Sens. 9, 649.

Damm, A., Erler, A., Hillen, W., Meroni, M., Schaepman, M.E., Verhoef, W., Rascher, U., 2011. Modeling the impact of spectral sensor configurations on the FLD retrieval accuracy of sun-induced chlorophyll fluorescence. Remote Sens. Environ. 115, 1882–1892.

Damm, A., Guanter, L., Paul-Limoges, E., van der Tol, C., Hueni, A., Buchmann, N., Eugster, W., Ammann, C., Schaepman, M.E., 2015. Far-red sun-induced chlorophyll fluorescence shows ecosystem-specific relationships to gross primary production: an assessment based on observational and modeling approaches. Remote Sens. Environ. 166, 91–105.

Donlon, C., Berruti, B., Buongiorno, A., Ferreira, M.H., Féménias, P., Frerick, J., Goryl, P., Klein, U., Laur, H., Mavrocordatos, C., Nieke, J., Rebhan, H., Seitz, B., Stroede, J., Sciarra, R., 2012. The Global Monitoring for Environment and Security (GMES) Sentinel-3 mission. Remote Sens. Environ. 120, 37–57.

Drusch, M., Moreno, J., Bello, U.D., Franco, R., Goulas, Y., Huth, A., Kraft, S., Middleton, E.M., Miglietta, F., Mohammed, G., Nedbal, L., Rascher, U., Schüttemeyer, D., Verhoef, W., 2017. The FLuorescence EXplorer Mission Concept 2014; ESA 2019's Earth Explorer 8. IEEE Trans. Geosci. Remote Sens. 55, 1273–1284.

ESA, 2015. Report for Mission Selection: FLEX, ESA SP-1330/2 (2 Volume Series). European Space Agency, Noordwijk, The Netherlands.

Guanter, L., Frankenberg, C., Dudhia, A., Lewis, P.E., Gómez-Dans, J., Kuze, A., Suto, H., Grainger, R.G., 2012. Retrieval and global assessment of terrestrial chlorophyll fluorescence from GOSAT space measurements. Remote Sens. Environ. 121, 236–251.

Guanter, L., Zhang, Y., Jung, M., Joiner, J., Voigt, M., Berry, J.A., Frankenberg, C., Huete, A.R., Zarco-Tejada, P., Lee, J.E., Moran, M.S., Ponce-Campos, G., Beer, C., Camps-Valls, G., Buchmann, N., Gianelle, D., Klumpp, K., Cescatti, A., Baker, J.M., Griffis, T.J., 2014. Global and time-resolved monitoring of crop photosynthesis with chlorophyll fluorescence. Proc. Natl. Acad. Sci. U. S. A. 111, E1327–E1333.

Guanter, L., Aben, I., Tol, P., Krijger, J.M., Hollstein, A., Köhler, P., Damm, A., Joiner, J., Frankenberg, C., Landgraf, J., 2015. Potential of the TROPOspheric Monitoring Instrument (TROPOMI) onboard the Sentinel-5 precursor for the monitoring of terrestrial chlorophyll fluorescence. Atmos. Meas. Tech. 8, 1337–1352.

Joiner, J., Yoshida, Y., Vasilkov, A.P., Yoshida, Y., Corp, L.A., Middleton, E.M., 2011. First observations of global and seasonal terrestrial chlorophyll fluorescence from space. Biogeosciences 8, 637–651.

Joiner, J., Yoshida, Y., Vasilkov, A.P., Middleton, E.M., Campbell, P.K.E., Yoshida, Y., Kuze, A., Corp, L.A., 2012. Filling-in of near-infrared solar lines by terrestrial fluorescence and other geophysical effects: simulations and space-based observations from SCIAMACHY and GOSAT. Atmos. Meas. Tech. 5, 809–829.

Joiner, J., Guanter, L., Lindstrot, R., Voigt, M., Vasilkov, A.P., Middleton, E.M., Huemmrich, K.F., Yoshida, Y., Frankenberg, C., 2013. Global monitoring of terrestrial chlorophyll fluorescence from moderate spectral resolution near-infrared satellite measurements: methodology, simulations, and application to GOME-2. Atmos. Meas. Tech. Discuss. 6, 3883–3930.

Liu, L., Zhang, Y., Jiao, Q., Peng, D., 2013. Assessing photosynthetic light-use efficiency using a solar-induced chlorophyll fluorescence and photochemical reflectance index. Int. J. Remote Sens. 34, 4264–4280.

Liu, X., Liu, L., Zhang, S., Zhou, X., 2015. New spectral fitting method for full-Spectrum solar-induced chlorophyll fluorescence retrieval based on principal components analysis. Remote Sens. 7, 10626–10645.

Liu, L., Liu, X., Hu, J., Guan, L., 2017. Assessing the wavelength-dependent ability of solar-induced chlorophyll fluorescence to estimate the GPP of winter wheat at the canopy level. Int. J. Remote Sens. 38, 4396–4417.

Malenovsky, Z., Mishra, K.B., Zemek, F., Rascher, U., Nedbal, L., 2009. Scientific and technical challenges in remote sensing of plant canopy reflectance and fluorescence. J. Exp. Bot. 60, 2987–3004.

Maxwell, K., Johnson, G.N., 2000. Chlorophyll fluorescence—a practical guide. J. Exp. Bot. 51, 659–668.

Meroni, M., Picchi, V., Rossini, M., Cogliati, S., Panigada, C., Nali, C., Lorenzini, G., Colombo, R., 2008. Leaf level early assessment of ozone injuries by passive fluorescence and photochemical reflectance index. Int. J. Remote Sens. 29, 5409–5422.

Meroni, M., Rossini, M., Guanter, L., Alonso, L., Rascher, U., Colombo, R., Moreno, J., 2009. Remote sensing of solar-induced chlorophyll fluorescence: review of methods and applications. Remote Sens. Environ. 113, 2037–2051.

Meroni, M., Busetto, L., Colombo, R., Guanter, L., Moreno, J., Verhoef, W., 2010. Performance of spectral fitting methods for vegetation fluorescence quantification. Remote Sens. Environ. 114, 363–374.

Middleton, E., Rascher, U., Corp, L., Huemmrich, K., Cook, B., Noormets, A., Schickling, A., Pinto, F., Alonso, L., Damm, A., Guanter, L., Colombo, R., Campbell, P., Landis, D., Zhang, Q., Rossini, M., Schuettemeyer, D., Bianchi, R., 2017. The 2013 FLEX—US airborne campaign at the Parker tract loblolly pine plantation in North Carolina, USA. Remote Sens. 9, 612.

Porcar-Castell, A., Tyystjarvi, E., Atherton, J., van der Tol, C., Flexas, J., Pfundel, E.E., Moreno, J., Frankenberg, C., Berry, J.A., 2014. Linking chlorophyll a fluorescence to photosynthesis for remote sensing applications: mechanisms and challenges. J. Exp. Bot. 65, 4065–4095.

Press, W.H., Teukolsky, S.A., Vetterling, W.T., Flannery, B.P., 2007. Numerical Recipes 3rd Edition: The Art of Scientific Computing. Cambridge University Press.

Rascher, U., Alonso, L., Burkart, A., Cilia, C., Cogliati, S., Colombo, R., Damm, A., Drusch, M., Guanter, L., Hanus, J., Hyvarinen, T., Julitta, T., Jussila, J., Kataja, K., Kokkalis, P., Kraft, S., Kraska, T., Matveeva, M., Moreno, J., Muller, O., Panigada, C., Pikl, M., Pinto, F., Prey, L., Pude, R., Rossini, M., Schickling, A., Schurr, U., Schuttemeyer, D., Verrelst, J., Zemek, F., 2015. Sun-induced fluorescence - a new probe of photosynthesis: first maps from the imaging spectrometer HyPlant. Glob. Chang. Biol. 21, 4673–4684.

Rinderle, U., Lichtenthaler, H.K., 1988. The chlorophyll fluorescence ratio F690/F735 as a possible stress indicator. In: Applications of Chlorophyll Fluorescene in Photosynthesis Research, Stress Physiology, Hydrobiology and Remote Sensing. Springer, pp. 189–196.

Rossini, M., Nedbal, L., Guanter, L., Ač, A., Alonso, L., Burkart, A., Cogliati, S., Colombo, R., Damm, A., Drusch, M., Hanus, J., Janoutova, R., Julitta, T., Kokkalis, P., Moreno, J., Novotny, J., Panigada, C., Pinto, F., Schickling, A., Schüttemeyer, D., Zemek, F., Rascher, U., 2015. Red and far red sun-induced chlorophyll fluorescence as a measure of plant photosynthesis. Geophys. Res. Lett. 42, 1632–1639.

Rossini, M., Meroni, M., Celesti, M., Cogliati, S., Julitta, T., Panigada, C., Rascher, U., van der Tol, C., Colombo, R., 2016. Analysis of red and far-red sun-induced chlorophyll fluorescence and their ratio in different canopies based on observed and modeled data. Remote Sens. 8, 412.

Sabater, N., Vicent, J., Alonso, L., Cogliati, S., Verrelst, J., Moreno, J., 2017. Impact of atmospheric inversion effects on solar-induced chlorophyll fluorescence: exploitation of the apparent reflectance as a quality indicator. Remote Sens. 9 (6), 622.

Schwarz, G., 1978. Estimating the dimension of a model. Ann. Stat. 6, 461–464.

Subhash, N., Mohanan, C., 1997. Curve-fit analysis of chlorophyll fluorescence spectra: application to nutrient stress detection in sunflower. Remote Sens. Environ. 60, 347–356.

Sun, Y., Frankenberg, C., Wood, J.D., Schimel, D.S., Jung, M., Guanter, L., Drewry, D.T., Verma, M., Porcar-Castell, A., Griffis, T.J., Gu, L., Magney, T.S., Köhler, P., Evans, B., Yuen, K., 2017. OCO-2 advances photosynthesis observation from space via solar-induced chlorophyll fluorescence. Science 358.

van der Tol, C., Verhoef, W., Timmermans, J., Verhoef, A., Su, Z., 2009. An integrated model of soil-canopy spectral radiances, photosynthesis, fluorescence, temperature and energy balance. Biogeosci. Discuss. 6, 3109–3129.

Van Wittenberghe, S., Alonso, L., Verrelst, J., Hermans, I., Delegido, J., Veroustraete, F., Valcke, R., Moreno, J., Samson, R., 2013. Upward and downward solar-induced chlorophyll fluorescence yield indices of four tree species as indicators of traffic pollution in Valencia. Environ. Pollut. 173, 29–37.

Verhoef, W., van der Tol, C., Middleton, E.M., 2018. Hyperspectral radiative transfer modeling to explore the combined retrieval of biophysical parameters and canopy fluorescence from FLEX – Sentinel-3 tandem mission multi-sensor data. Remote Sens. Environ. 204, 942–963.

Verrelst, J., Rivera, J.P., van der Tol, C., Magnani, F., Mohammed, G., Moreno, J., 2015. Global sensitivity analysis of the SCOPE model: what drives simulated canopy-leaving sun-induced fluorescence? Remote Sens. Environ. 166, 8–21.

Verrelst, J., van der Tol, C., Magnani, F., Sabater, N., Rivera, J.P., Mohammed, G., Moreno, J., 2016. Evaluating the predictive power of sun-induced chlorophyll

fluorescence to estimate net photosynthesis of vegetation canopies: a SCOPE modeling study. Remote Sens. Environ. 176, 139–151.
Widlowski, J.L., Pinty, B., Lopatka, M., Atzberger, C., Buzica, D., Chelle, M., Disney, M., Gastellu-Etchegorry, J.P., Gerboles, M., Gobron, N., Grau, E., Huang, H., Kallel, A., Kobayashi, H., Lewis, P.E., Qin, W., Schlerf, M., Stuckens, J., Xie, D., 2013. The fourth radiation transfer model intercomparison (RAMI-IV): proficiency testing of canopy reflectance models with ISO-13528. J. Geophys. Res. Atmos. 118, 6869–6890.
Wolanin, A., Rozanov, V.V., Dinter, T., Noël, S., Vountas, M., Burrows, J.P., Bracher, A., 2015. Global retrieval of marine and terrestrial chlorophyll fluorescence at its red peak using hyperspectral top of atmosphere radiance measurements: feasibility study and first results. Remote Sens. Environ. 166, 243–261.
Zhang, Y., Guanter, L., Berry, J.A., Joiner, J., van der Tol, C., Huete, A., Gitelson, A., Voigt, M., Kohler, P., 2014. Estimation of vegetation photosynthetic capacity from space-based measurements of chlorophyll fluorescence for terrestrial biosphere models. Glob. Chang. Biol. 20, 3727–3742.
Zhang, Y., Guanter, L., Berry, J.A., van der Tol, C., Yang, X., Tang, J., Zhang, F., 2016. Model-based analysis of the relationship between sun-induced chlorophyll fluorescence and gross primary production for remote sensing applications. Remote Sens. Environ. 187, 145–155.
Zhao, F., Guo, Y., Verhoef, W., Gu, X., Liu, L., Yang, G., 2014. A method to reconstruct the solar-induced canopy fluorescence Spectrum from hyperspectral measurements. Remote Sens. 6, 10171–10192.
Zhao, F., Guo, Y., Huang, Y., Reddy, K.N., Zhao, Y., Molin, W.T., 2015a. Detection of the onset of glyphosate-induced soybean plant injury through chlorophyll fluorescence signal extraction and measurement. J. Appl. Remote. Sens. 9, 097098-1–097098-12.
Zhao, F., Li, Y., Dai, X., Verhoef, W., Guo, Y., Shang, H., Gu, X., Huang, Y., Yu, T., Huang, J., 2015b. Simulated impact of sensor field of view and distance on field measurements of bidirectional reflectance factors for row crops. Remote Sens. Environ. 156, 129–142.
Zhao, F., Dai, X., Verhoef, W., Guo, Y., van der Tol, C., Li, Y., Huang, Y., 2016. FluorWPS: a Monte Carlo ray-tracing model to compute sun-induced chlorophyll fluorescence of three-dimensional canopy. Remote Sens. Environ. 187, 385–399.